Green Chemistry

Accepted Manuscript

ROYAL SOCIETY OF CHEMISTRY

www.rsc.org/greenchem

Cite this: DOI: 10.1039/c0xx00000x

www.rsc.org/xxxxxx

ARTICLE TYPE

Supramolecular–directed novel superparamagnetic 5'-adenosine monophosphate templated β-FeOOH hydrogel with enhanced multi-functional properties

Anil Kumar* and Sudhir Kumar Gupta

Received (in XXX, XXX) Xth XXXXXXXXX 20XX, Accepted Xth XXXXXXXXX 20XX
DOI: 10.1039/b000000x

The present work describes the synthesis and properties of 5'-AMP mediated porous superparamagnetic β-FeOOH hydrogel employing biocompatible components. For the optimized 5'-AMP mediated β-FeOOH hydrogel containing 2.5 mM of 5'-AMP (SP4H), initially colloidal nanoparticles are produced, which in the process of self-assembly reorganize to form hydrogel. The process of gelation is found to be controlled by the change in concentration of 5'-AMP, pH and temperature. The presence of β-FeOOH in hydrogel sample is indicated by Raman, UV-Vis-NIR, IR spectroscopy, XPS and SAED analysis. FESEM, AFM and TEM analysis of this sample reveal it to be porous, which is also indicated by its high BET surface area (215 $m^2 g^{-1}$) as compared to that of untemplated β-FeOOH. Zeta potential (ζ) measurements show the fresh nanoparticles to be fairly stable with a ζ-value of ~45 mV, which upon gelation becomes negatively charged with a change in ζ value to ~-35 mV. The occurrence of gelation is assigned to the change in interaction between the core-β-FeOOH and 5'-AMP in the shell. The FTIR analysis show interactions through pyrimidine ring, in plane C(8)H and PO_3^{2-} are responsible for gelation. The 5'-AMP templated β-FeOOH hydrogel exhibits superparamagnetic behavior from 300 to 50 K associated with more than 75% increase for room temperature magnetization (3.4 emu/g) as compared to the bare β-FeOOH (1.9 emu/g) at 7 T. Unlike bare 5'-AMP mediated hydrogel, as synthesized 5'-AMP templated β-FeOOH hydrogel employs more than an order of magnitude lower concentration of 5'-AMP and display enhanced multifunctional properties. The use of non-toxic precursors for synthesizing 5'-AMP mediated β-FeOOH hydrogel in aqueous medium having potential for biomedical applications; suggest it to be the green material.

Introduction

In recent years iron oxide nanostructures have drawn considerable attention due to their tuneable magnetic behavior and characteristic higher absorption coefficient in UV-Vis region besides being economical, easily available and biocompatible.[1-5] The chemical approaches developed over the last one decade allow the synthesis of nanostructures in different dimensionalities/morphologies such as nanoparticles (NPs), nanorods, nanowires, nanofibers, nanotubes and nanocubes for manipulating their properties.[6-10] The extensively investigated phases of oxides and oxyhydroxides of iron for various applications are: iron oxides (α-Fe_2O_3, γ- Fe_2O_3 and Fe_3O_4) and iron oxyhydroxides (α-FeOOH, β-FeOOH and γ-FeOOH). These nanostructures are finding wide ranging applications in the areas of data storage, magnetic devices, photocatalysis, catalysis, adsorption and nanobiotechnology.[4,7,11-17]

Department of Chemistry, Indian Institute of Technology Roorkee, Roorkee – 247667, India
E-mail: anilkfcy@iitr.ernet.in; Fax: +91-1332-273560

In particular for catalytic/photocatalytic, environmental and biomedical applications, the porous morphology become important as regard to their usage for loading and controlled release of desired molecules.

Lately a number of investigations have focused on β-FeOOH (akaganeite) nanostructures having a band gap of 2.12 eV and is different from the other phases of iron oxides and oxyhydroxides as regards to the arrangement of the anions in bcc structure, since all other phases of iron oxide or oxyhydroxide have either hcp or ccp structure.[2] In the bulk phase it is known to possess the monoclinic or tetragonal geometry with a wide tunnel like structure in which Cl^- ions are stabilized by hydrogen bonding[2] and very similar structure is reported to be retained in its nanodimensions.[18] Lithium ions can be intercalated and extracted freely through these tunnels during the process of charging and discharging and thus making it a potential electrode material for Li-ion batteries.[18] It has also been explored for toxic ion removal, catalysis and ion-exhange.[19-21]

The integration of biomolecule with inorganic nanomaterials

has been extensively explored in recent years to manipulate various physical and chemical properties *viz*. solubility, optical and magnetic property due to their surface passivation, control of surface spin and morphology.[22-25] For the biomedical applications it will be interesting to template β-FeOOH with biocompatible capping agents. Nucleotides are the important components of nucleic acids (DNA/RNA) containing large functionalities to undergo supramolecular interaction(s) with the core material and among its molecules present in the shell.[22] Apart to these, β-FeOOH nanoparticles exhibit low toxicity[26,27] and superparamagnetic behavior suggesting their applications in magnetic resonance imaging, targeted drug delivery, cell labeling, magnetic separation and hyperthermia.[4,28-30]

In the present study we have employed 5'-adenosine monophoshate (5'-AMP) (Fig. 1) having large chemical functionalities (–C=O, $–NH_2$, –C=N–, –C–O– of sugar, –O–H of sugar, –P–O– 5'-sugar, $–PO_3^{2-}$, sugar ring and pyrimidine and imidazole) as templating agent. 5'-AMP is responsible for the synthesis of complex molecules responsible for storage of energy in living organisms. We have come across only one report in the literature on the formation of hydrogels involving bare adenosine monophosphate using enzyme and gelator (alkaline phosphotase and naphthalene-Phe-Phe-Lys, a tripeptide derivative), which have been used to generate new biomaterials.[31] However, we did not find any report on the formation of hydrogel using 5'-AMP and iron oxide(s). 5'-AMP may manipulate the morphology of β-FeOOH nanostructures by binding to the metal ion through its functionalities. Further, the interaction of nucleotide can be influenced by change in the reaction parameters like pH, temperature and chemical environment/medium. These parameters have been explored to control the morphology and features of 5'-AMP mediated β-FeOOH nanostructures and also to produce hydrogel in the process of self-assembly. As synthesized β-FeOOH hydrogel containing environment friendly biocompatible precursors having high porosity, NIR absorption, enhanced magnetization with superparamagnetic behavior qualifies to be green material with potential for biomedical applications. Such material may serve better utility as regards to the suggested applications compared to that synthesized using bare 5'-AMP mediated hydrogel, which lack these characteristic features.[31] Moreover, the method used for its synthesis fits well with the green approach as it neither employs any surfactant nor involves the consumption of any solvent.

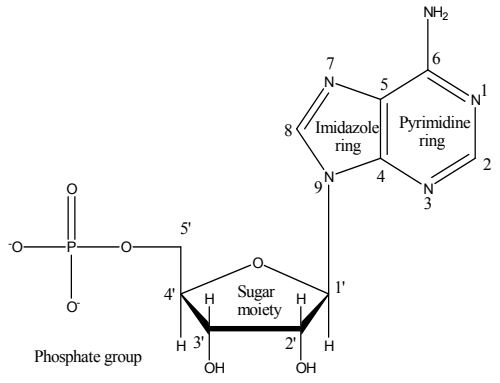

Fig. 1 Structure of 5'-adenosine monophosphate.

2. Experimental Section

2.1 Reagents.

$FeCl_3$, KBr (Merck, AR); 5'-adenosine monophosphate disodium salt (SRL, AR); $HClO_4$ (Qualigens, AR); NaOH, HCl (s-d Fine chemicals, AR), carbon coated copper grids for TEM (Ted Pella Inc., USA); dialysis tubing (seamless cellulose tubing) and their closures (Sigma) were used. All the reagents were used without any further purification. All solutions were prepared freshly in Millipore water (Bedford, MA, USA).

2.2 Equipment.

Electronic spectra of the samples were recorded in UV–Visible (200-800 nm) and UV-Vis-NIR (200-1200 nm) ranges on Shimadzu 2100S and Perkin Elmer Lambda 950 UV-Vis-NIR spectrophotometers, respectively. Raman spectra of the various samples were recorded on an *inVia* Raman spectrophotometer with serial no. 021R88 and H33197 equipped with a confocal microscope and 514 nm Ar ion laser having spectral resolution of 1 cm^{-1}. The colloidal stability of the 5'-AMP templated β-FeOOH nanostructures were analyzed on a Zetasizer ZS90 procured from Malvern Instruments, UK by using 632 nm He-Ne laser as light source. The morphology and the elemental analysis of the as synthesized nanostructures were performed on a FEI-QUANTA 200F field emission scanning electron microscope (FESEM) equipped with energy dispersive x-ray analysis (EDX) accessory by applying an acceleration voltage of 20 kV. The surface morphology of these samples was further analyzed by recording their two- and three-dimensional images on an NTEGRE (NTMDT) atomic force microscope (AFM) in semi-contact mode using tip with curvature radius of 10 nm. It has a resolution of 0.2 nm in x and y axes and of 0.04 nm along z– axis. The electron micrographs and selected area electron diffraction (SAED) measurements of the samples were carried out on a FEI, TECNAI transmission electron microscope operating at an accelerating voltage of 200 kV. The porosity of the FD gel sample was analyzed by recording its surface area and pore volume on a NOVA 2200e High Speed Automated Surface Area Analyzer by using Nova Win software. Fourier Transform Infra-red (FTIR) spectra of powdered samples were recorded on a Thermo Nicolet Nexus (FTIR) spectrophotometer in KBr medium in the mid-IR range (4000-400 cm^{-1}). The X–ray photoelectron spectral analysis of the sample was recorded on a custom–built laboratory version ambient pressure photoelectron spectrometer (Lab–APPES) at 1 $\times$ 10^{-10} mbar pressure.[32] The magnetic measurements were performed at various temperatures and applied magnetic fields on a Quantum Design MPMS-XL superconducting quantum interference device (SQUID) magnetometry and vibrating sample magnetometer option in Physical Properties Measurement System (PPMS) from Quantum Design, USA. The amount of 5'-AMP present in the samples was estimated by performing elemental analysis Vario MICRO cube CHNS analyzer from Elementar by digesting sample to 1200 ºC. The hydrolysis was carried out in a round bottom flask by heating the reaction mixture in a silicon oil bath operated at 230 V, 500W and 50 Hz equipped with a PID controller procured from Medica Instruments MFG., Co. The solvent was removed from the colloidal samples by using Buchi Rotavapor R-114 equipped with water bath B-480. These samples were dried in vacuum oven from Labtech, Daihan Labtech Co.

Ltd. The pH measurements of the various samples were performed on a pH510 pH meter from Eutech instruments. The hydrogel samples were freeze dried and then lyophilized in a Lyophilyzer equipped with Pirani gauge and a digital temperature controller from Biosync Teknology, Delhi.

2.3 Methodology

2.3.1 Synthesis of 5'-AMP-templated colloidal β-iron oxyhydroxide.

5'-AMP templated colloidal β-FeOOH nanostructures were synthesized by adding 0.49 g of $FeCl_3.6H_2O$ in 100 ml (~ 30 mM) aqueous solutions containing the varied amount of 5'-AMP (0.5 – 5.0 mM). The solutions were heated with refluxing at 100°C in a silicon oil bath for 6 h under continuous stirring and, thereafter, cooled to the room temperature. The resulting solutions were dialyzed for 12-15 h for the removal of excess Fe^{3+} and 5'-AMP. The resulting colloidal samples were stored at room temperature. At higher concentrations of 5'-AMP (> 1 mM), the colloidal solution undergoes spontaneous transformation to yield gel within a period of about 10 days. The optical spectra of the gel samples were recorded immediately after shaking them so as to transform it into the colloidal solution. These samples, however, exhibited scattering of some light. The gelified samples were freeze dried and then lyophilized to obtain the solid freeze dried (FD) gel for the ir, xps and magnetic measurements.

In a control experiment β- iron oxyhydroxide sample was also prepared in the absence of 5'-AMP (SB) by employing similar experimental conditions, which resulted in a turbid suspension. The β-FeOOH samples containing varied amount of 5'-AMP (mM) have been abbreviated as: SB (0.0), SP1 (0.5), SP2 (1.0), SP3 (1.5), SP4 (2.5) and SP5 (5.0) and the respective aged samples as SP1A, SP2H, SP3H, SP4H and SP5H, respectively. It may be noted that the hydrogel was formed only for SP2, SP3, SP4 and SP5. In case of SP2, it took about one month for the formation of hydrogel, whereas for all other samples the duration was ≤ 10 days.

2.3.2 Preparation of Samples for Analysis by FESEM, TEM, AFM, Zetasizer, Surface Area Analyzer, XPS and SQUID

Samples for FESEM and AFM analyses were prepared by applying a drop of dilute colloidal solution on the glass substrate, which was dried at 30 °C in dark. For FESEM analysis gold was coated on the surface of the sample in order to make it conducting. For TEM analysis a small drop of dilute solution was applied on to a carbon coated copper grid (G-200) (3.05 mm). Excess water from the copper grid was removed by tissue paper and was kept in dark at room temperature prior to its examination. For zeta potential measurements were made in a clear disposable cuvette having folded capillary and the data obtained were analyzed by using DTS Nano software. For the analysis of magnetic measurements, a correction to the amount of β-FeOOH present in these samples was made by estimating the 5'-AMP present in these samples. Its estimation was carried out by performing dialysis till no 5'-AMP could be eluted. The amount of eluted 5'-AMP was determined by CHNS analyzer. The freeze dried hydrogel samples were used as such for the surface area, XPS and magnetic measurements.

3. Results

3.1 Raman Spectroscopy

As synthesized samples containing different amount of 5'-AMP were further characterized by Raman spectroscopy for identification of iron oxide phase (Fig. 2). The Raman peaks (cm^{-1}) in these samples were observed at: 307, 387 and 721 along with a broad peak beyond 1200. From the literature data these peaks were found to match with the vibrational bands reported for β-FeOOH phase.[33,34] The peaks observed at 243, 823, 1321, 1391, 1421, 1506 and 1560 cm^{-1} appear to have arisen from the free 5'-AMP.[35] At higher concentrations of 5'-AMP (> 1.0 mM), the vibrational bands due to both β-FeOOH phase and 5'-AMP become more prominent and beyond [5'-AMP] (>2.5 mM) the intensity due to 5'-AMP become more pronounced as compared to that of β-FeOOH phase. Obviously at this concentration of 5'-AMP the peaks due to β-FeOOH are masked.

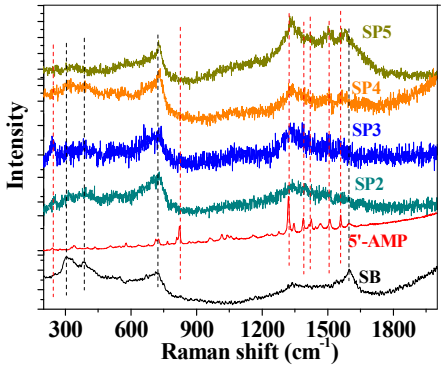

Fig. 2 Raman spectra of the fresh samples containing different concentration of 5'-AMP along with SB and 5'-AMP blank.

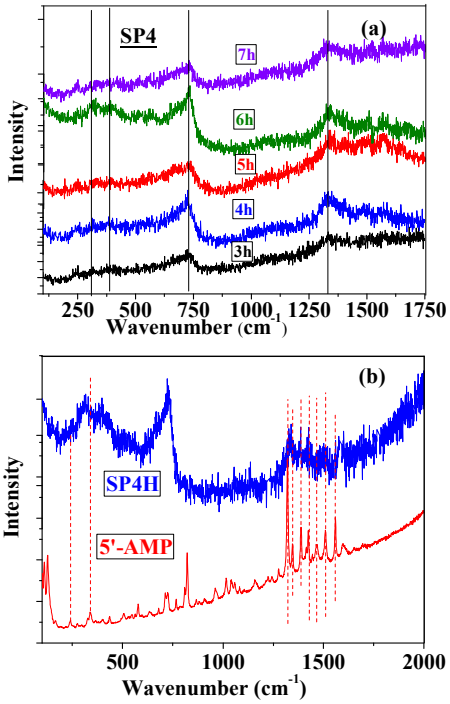

Fig. 3 (a) Raman spectra of the SP4 recorded after different time intervals of heating with refluxing and (b) Raman spectra of SP4H (for comparison Raman spectra of 5'-AMP has also been included).

The reflux time for the formation of 5'-AMP mediated β-FeOOH was optimized by recording the Raman spectra of SP4 refluxed for different durations (Fig. 3 (a)) and was followed by monitoring the intensity of peaks due to β-FeOOH at 307, 387,

723 and broad peak beyond 1200 cm^{-1}. From these studies it is noted that the peaks due to β-FeOOH phase were found to be the most intense after 6 h of refluxing. Any lesser or higher timings of reflux, however, yielded less intense peaks due to β-FeOOH phase.

For longer refluxing time (> 6 h), the peaks due to β-FeOOH became less intense. Therefore, in all further studies reflux time was kept at 6 h. In previous studies also β-FeOOH has been observed to undergo transformation into α-Fe_2O_3 phase upon refluxing for longer periods.[36,37] The Raman spectrum for the 5'-AMP mediated β- FeOOH hydrogel sample SP4H is shown in Fig. 3 (b).

It displays very similar spectral features as observed for SP4 besides having some additional peaks due to 5'-AMP getting prominent.

3.2 UV-Vis spectroscopy-

UV-Vis-NIR optical absorption spectra of fresh colloidal samples were recorded as a function of concentration of 5'-AMP along with the absorption spectra of pure 5'-AMP (Fig. 4 (a)). At low concentrations of 5'-AMP it displays four broad bands in UV-Visible region at 254, 302, 347 and 479 nm, and a broad band in NIR range at about 890 nm, where 5'-AMP does not have any absorption (Figs. 4 (a) and (b)). An increasing addition of 5'-AMP reduces the absorption coefficient due to all these bands.

Interestingly, in UV region at 260 nm where 5'-AMP has higher absorption, the absorption coefficients due to these samples are reduced significantly. Aging of these samples recorded for a period of 9 days shows a decrease in the optical absorption in the UV-visible range from 200 to 430 nm associated with a simultaneous increase in absorption in visible–NIR range starting from 430 to 1200 nm with a broad absorption band peaking at about 850 nm (Figs. 5 (a) and (b)). These changes exhibit an isosbestic point at about 430 nm (Fig. 5 a).

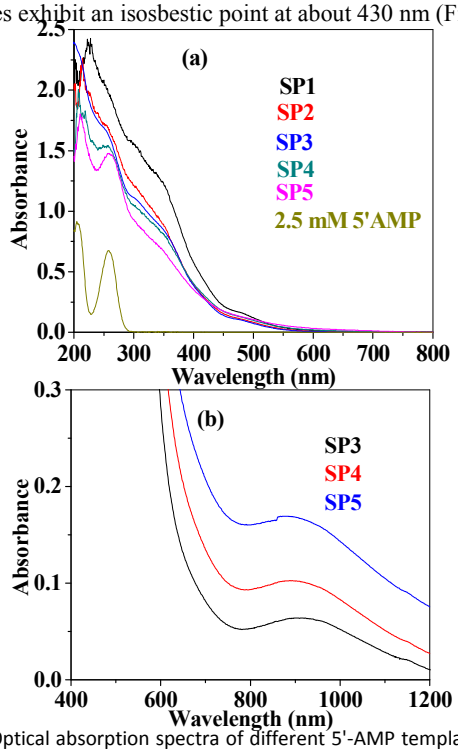

Fig. 4 Optical absorption spectra of different 5'-AMP templated colloidal β-FeOOH samples at pH 4 in (a) UV-Visible region and (b) NIR region.

The peak at 254 nm has been attributed to the ligand to metal charge transfer (LMCT) transition arising from the ligand O_2^- to Fe^{3+} metal centre. The bands at 302 an 347 nm may be assigned to the ligand field transition of Fe^{3+}, whereas the broad band with a relatively lower absorption coefficient in the range of 450-500 nm can be assigned to transition corresponding to magnetically coupled Fe^{3+} cations. The absorption in the NIR region at about 890 nm is understood to arise due to ligand field transition due to Fe^{3+} cations.[38,39]

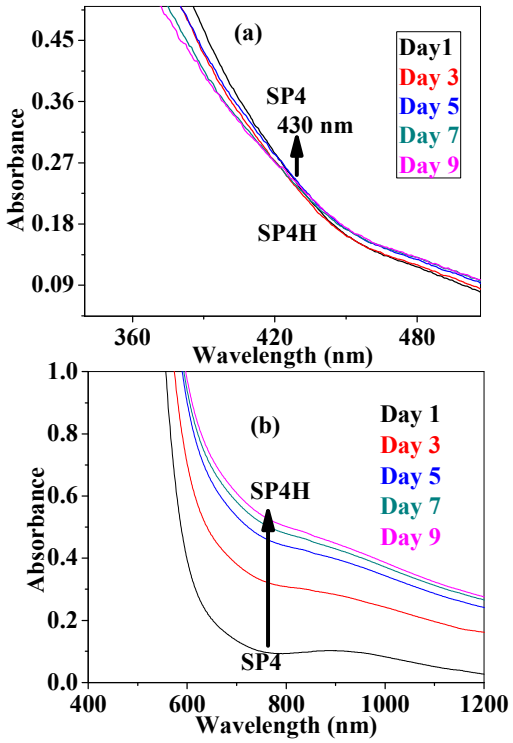

Fig. 5 Absorption spectra of the SP4 samples upon aging in the UV-Vis region (a) and UV-Vis-NIR region (b).

3.3 Zetasizer analysis

In the optimization process the gelation was visually observed to take place beyond 1 mM of 5'-AMP at a relatively faster pace. For analyzing the mechanism of gelation the ζ-potential of these samples were recorded at pH 4.0 as a function of [5'-AMP] and are shown in Fig. 6. From this plot it is apparent that ζ-potential starts taking a plateau value beyond 1.5 mM of 5'-AMP.

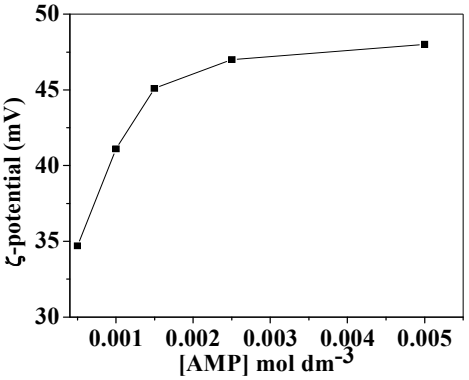

Fig. 6 Variation of ζ-potential of fresh colloidal 5'-AMP mediated β-FeOOH samples at pH 4 as a function of [5'-AMP].

The gelation period (days) for different concentrations (mM) of 5'-AMP was determined by the duration for attaining the saturation in ζ-potential and varied in the order: SP2H (~30) > SP3H (10) > SP4H (~8) > SP5H (~8). For SP4, the process of gelation was monitored for 10 days at an interval of a day. Interestingly, the aging resulted in an increase in the pH, which caused a regular reduction in ζ-potential (Fig. 7). After about 4 days, the pH increased to about 5.5 at which the value of ζ-potential was observed to be zero (point of zero charge). Thereafter, the magnitude of ζ-potential becomes increasingly negative and within 10 days it gives a fairly negative value of -34.6 mV, which remained constant for much longer period. Thus, suggesting the negatively charged colloidal dispersion to be fairly stable.

The complex change in the variation of pH and ζ-potential was further examined by designing an experiment in which the pH of the sol was varied manually (Fig. 8). Interestingly, the variation of the ζ-potential with pH followed a very similar trend as observed above from Fig. 7 and the point of zero charge was obtained to be around 6.1. This experiment evidently reveals that a change in pH of the colloidal system is responsible for the gelation.

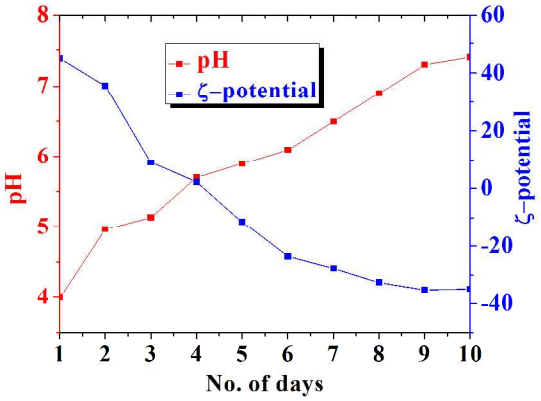

Fig. 7 Variation of pH and ζ-potential upon aging for SP4.

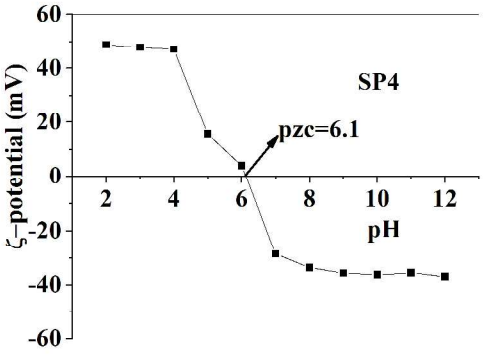

Fig. 8 Variation of ζ-potential with pH for SP4.

3.4 FESEM analysis

FESEM images of SP3, SP4 and SP5 are shown in Fig. 9. For SP4 and SP5 it produced nanochains consisting of NPs joined together, forming a network of coiled nanochains. A careful examination of these FESEM images indicates a regular decrease in the size from SP3 to SP5. SP3 shows the presence of both nanoparticles and nanorods, whereas in case of SP4 the formation of organized entangled chains consisting of nanoparticles becomes prominent and the size of the particles is also slightly reduced. The image of SP5 is very similar to SP4 except depicting a further decrease in the size of the nanoparticles.

The morphological changes in these samples upon aging were also monitored (Fig. 10). Upon aging the porosity is generated in these nanostructures and follows the order SP5H<SP3H<SP4H. In case of SP5 the nanochains get aggregated to exhibit the rod type of nanostructures (Fig. 10 (c)). An EDAX analysis of pores in SP4H indicates that the amount of iron in the pore is much less as compared to those on the surface of the particle (Fig. S1). It suggests that inside the pores iron might have been contributed from the background of the deposited film.

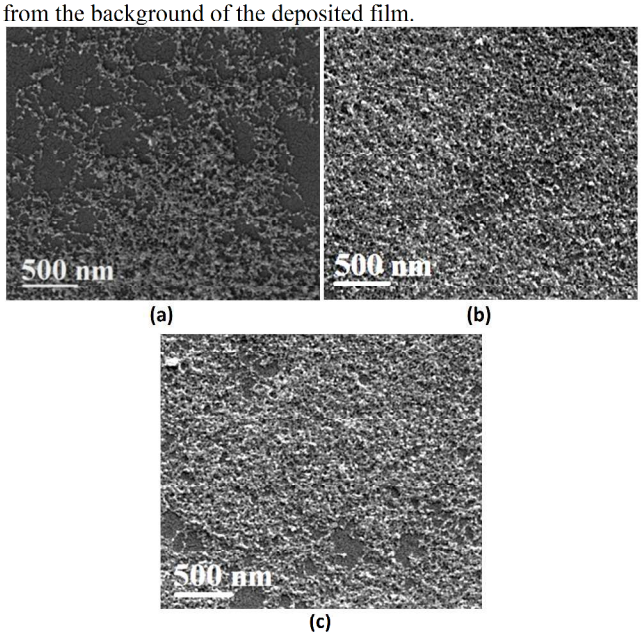

Fig. 9 FESEM images of the fresh 5'-AMP template β-FeOOH samples: (a) SP3, (b) SP4 and (c) SP5.

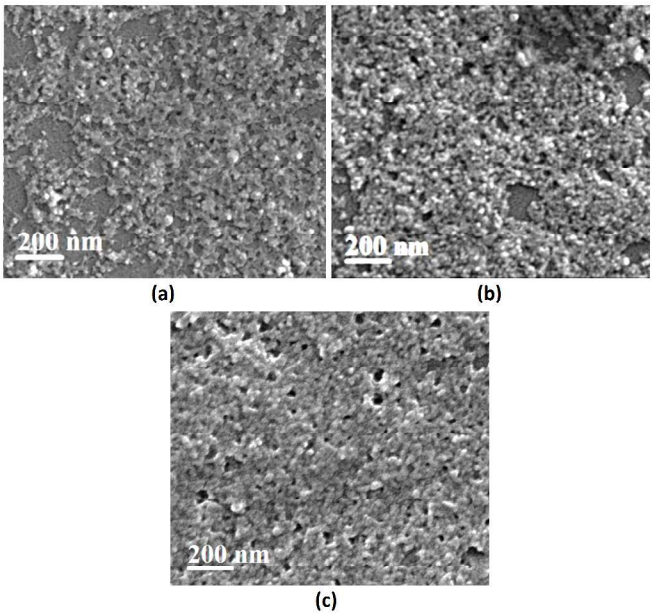

Fig. 10 FESEM image of the 5'-AMP templated β-FeOOH hydrogel samples: (a) SP3H, (b) SP4H and (c) SP5H.

3.5 TEM analysis

The TEM micrographs of SP3 SP4 and SP5 are shown in Fig. 11. The analysis of TEM micrograph of SP3 shows the presence of both NPs as well as nanorods, whereas, in case of SP4 and SP5 it exhibits the formation of chain like structure consisting of both NPs and nanorods. The size distribution histograms of the nanostructures in SP3–SP5 have been shown in Figs. 11 (e), S2 and S3. The average diameter (size distribution) of the spherical nanoparticles in different samples is – SP3: 5 nm (2.5-7.5 nm); SP4: 5 nm (2.5-7.5 nm) and SP5: 3 nm (1.5-5.5 nm). The dimensions of the nanorods (size distribution) are – SP3: 22.5 nm (10-40 nm) × 4.5 nm (1.5-6.5 nm); SP4: 15 nm (7.5-27.5 nm) × 4 nm (2.5-5.5 nm) and SP5: 15 nm (10-40 nm) × 4 nm (1.5-5.5 nm).

SAED analysis of SP4 exhibits the presence of diffused rings indicating the sample to be amorphous in nature (Fig. 11 (d)). The indexing of this SAED pattern matches to the planes (103), (400), (114) and (512) planes corresponding to β–FeOOH (JCPDS file no. 80–1770).

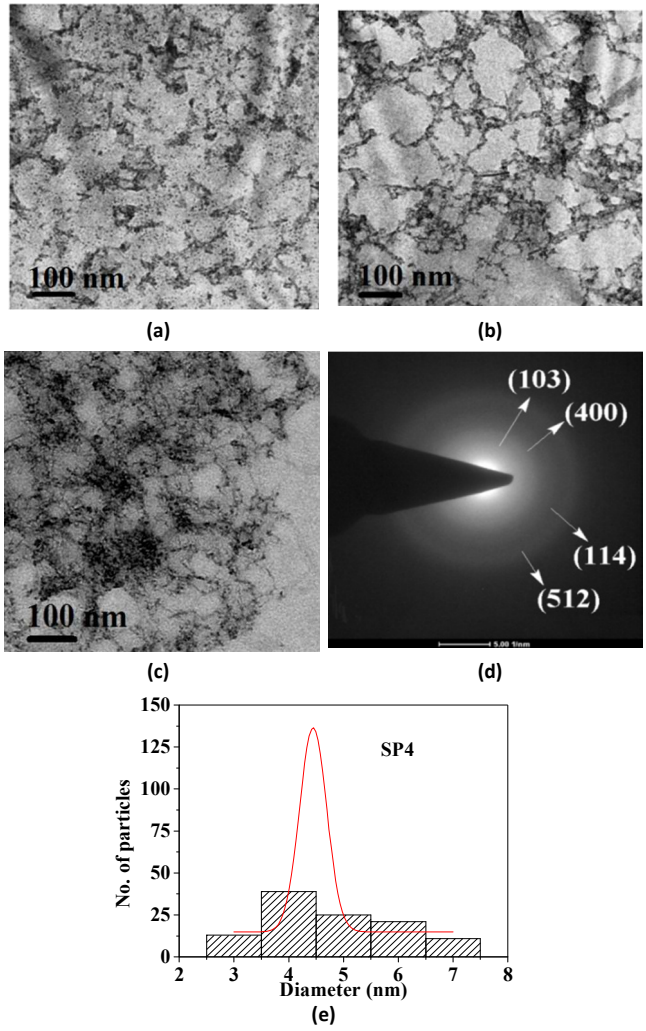

Fig. 11 TEM images of the fresh samples: SP3 (a), SP4 (b) and SP5 (c) along with the diffraction pattern (d) of SP4 and its size–distribution plot (e).

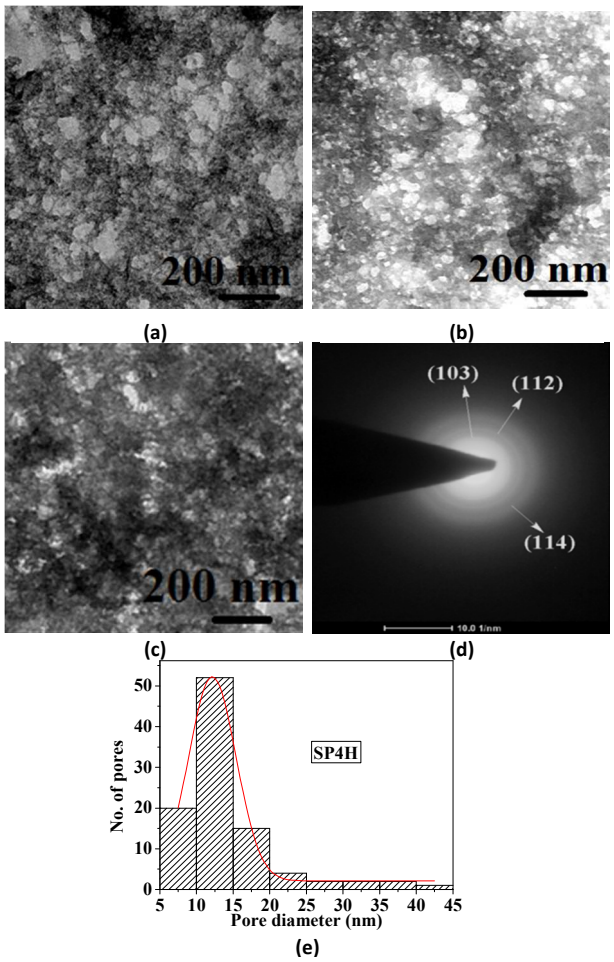

Fig. 12 TEM images of the hydrogel samples SP3H (a), SP4H (b) and SP5H (c) along with the SAED image of SP4H (d) and pore size distribution of SP4H (e).

The morphological changes were also monitored upon aging of these samples (Fig. 12). TEM micrographs reveal that upon aging the folding of nanochains through supramolecular interactions of template to generate the pits and porosity for all the samples with the highest porosity in SP4H (Fig. S4). The SAED pattern of SP4H (Fig. 12 (d)) shows the presence of diffused ring structure and indexing of this pattern also shows the reflections from the planes corresponding to β–FeOOH phase as observed for the fresh sample SP4. The size (size distribution) of pores from this image was estimated to be 12.5 nm (5 to 45 nm).

3.6 BET Surface Area Analysis

The porosity of FD-SP4H was further examined by recording surface area by using five-point BET method upon degassing it for 3 h at 100 °C under vacuum, which was followed by adsorption of N_2 gas. Its surface area was found to be 215 m^2 g^{-1}, which is about more than 2.5 times higher than blank SB[36] (82.8 m^2 g^{-1}) indicating FD-SP4H to be porous. More over pore volume analysis by BJH method showed it to have the pore volume of 0.23 ± 0.01 cc/g.

3.7 AFM analysis

To further analyze the morphological changes AFM images of all the hydrogel samples were recorded. AFM images of β-FeOOH

samples containing different concentration of 5'-AMP are presented in Figs. S5 and 13. In the fresh samples (SP3, SP4 and SP5), an increase in 5'-AMP is found to cause a reduction in the average surface roughness* of the nanoparticles and particles undergo aggregation to generate porosity.

The aging of these samples produces more organized porous structure for SP3H and SP4H (Fig. 13). For SP3H the organization of NPs exhibits a small number of pores with an average surface roughness of 28 nm. AFM image of SP4H produces relatively more pits on the surface of particles with increased porosity and the average surface roughness* is increased to 30 nm. Whereas, in case of SP5H, aggregated nanorods associated with a reduction in the porosity are formed. The average surface roughness of this sample is reduced to 25 nm. The porosity induced in SP4H has been shown through the line scan along x and y axes and the respective plots have been shown in Fig. 14.

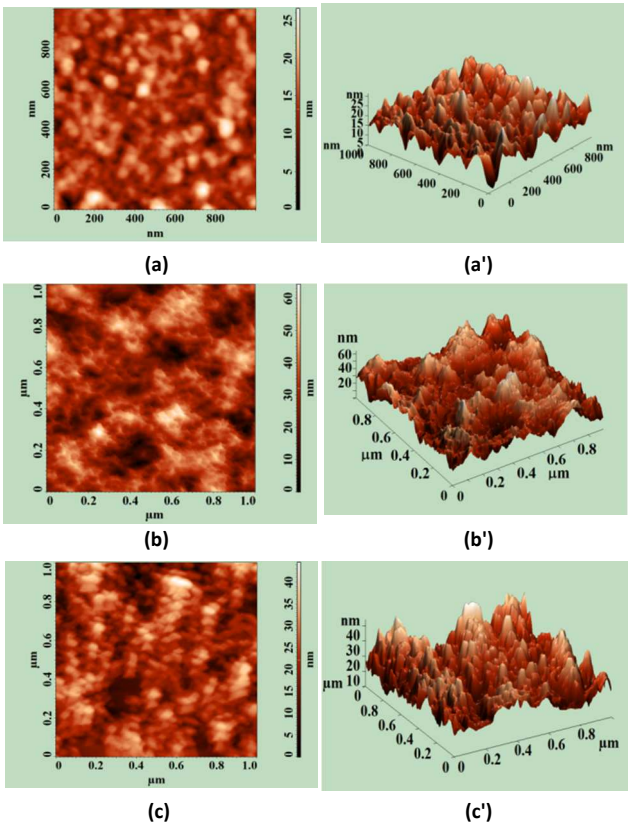

Fig. 13 AFM images and the respective 3-D image of the different hydrogel samples: SP3H (a) and (a'); SP4H (b) and (b') and SP5H (c) and (c') respectively.
*Average surface roughness (distribution): SP3H-12 nm (5-25 nm); SP4H-35 nm (10 to 60 nm) and SP5H-22 nm (5 to 35 nm).

The observed morphological change in case of hydrogel samples might have arisen due to increased supramolecular interactions among the functionalities of 5'–AMP and β–FeOOH in the process of self–assembly. These changes in the morphology of different β–FeOOH nanostructures for varied concentrations of 5'-AMP along with the self-assembly has been presented in Scheme 1. It clearly shows that addition of 5'-AMP influences the process of nucleation and growth by binding with β–FeOOH. At lower [5'-AMP], only some of the β-FeOOH molecules bind to 5'-AMP and might still grow through the other uncomplexed ends of β-FeOOH. Whereas, at higher [5'-AMP], more molecules of 5'-AMP are likely to bind and inhibit the growth of the building block, thereby producing spherical nanoparticles (Scheme 1b). The formation of gel can be understood due to the increased supramolecular interactions among different building blocks involving 5'-AMP - 5'-AMP and 5'-AMP – β-FeOOH.

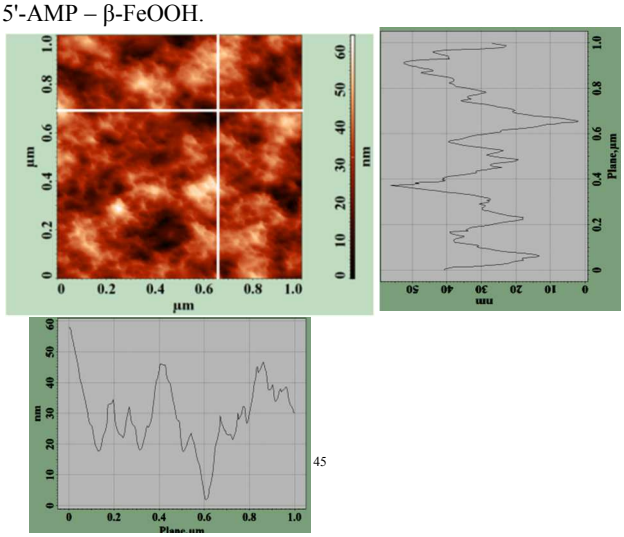

Fig. 14 Line scan profiles of the SP4H sample along x and y– axes.

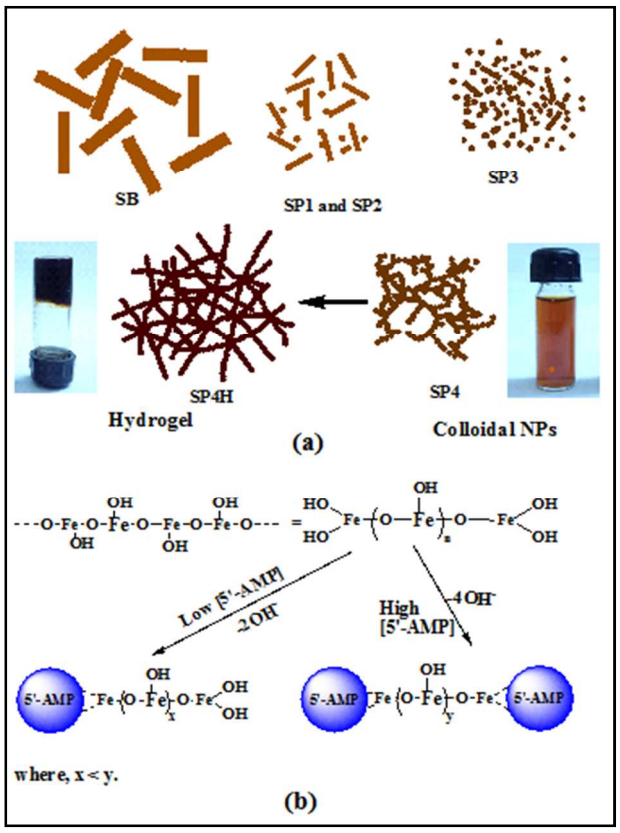

Scheme 1 Presenting the effect of 5'-AMP concentration on the morphology and nature of β-FeOOH nanostructures.

From the morphological studies it is apparent that the porosity is the maximum for SP4H, which is an interesting finding as regards to their usage for biomedical applications. Therefore, all further studies have been restricted to the analysis of SP4 and SP4H.

3.8 FTIR Spectra

Fig. 15 presents the IR spectra of SB, SP4, and SP4H along with that of pure 5'-AMP recorded under identical experimental conditions and the observed spectral data are given in Table S1. The IR spectrum of SP4 exhibited characteristic peaks (cm^{-1}) for O-H···Cl deformation at 830 and Fe-O-Fe stretching at 702 and 648, similar to those reported earlier for β-FeOOH.[2]

The IR spectrum of 5'-AMP was very similar to that of reported in the literature[40] which exhibited peaks at (cm^{-1}): 1655, 1610, 1576, 1510, 1480, 1423, 1394, 1339, 1302, 1255, 1216, 1151, 1115, 1086, 1029, 987, 873 and 810 (Table S1).

Interestingly, in SP4 several peaks due to different functionalities (absorption frequency in cm^{-1}) of 5'-AMP such as: sugar ring (1151), C(8)N(9) stretching (1029), ring mode (629), -P-O (768), disappeared and C-4-C-5 skeletal vibrations (1602), pyrimidine ring vibration (1583), C(6)N(1) bending (1407), imidazole (1383) and sugar ring (857) showed significant change(s) in their position and/or shape. These observations evidently suggest an interaction of 5'-AMP with β-FeOOH in SP4. In SP4H the peaks due to (cm^{-1}): pyrimidine ring vibration (1574), in plane C(8)H bending (1211), PO_3^{2-} symmetric stretching (982), get slightly red shifted with a reduction in the intensity.

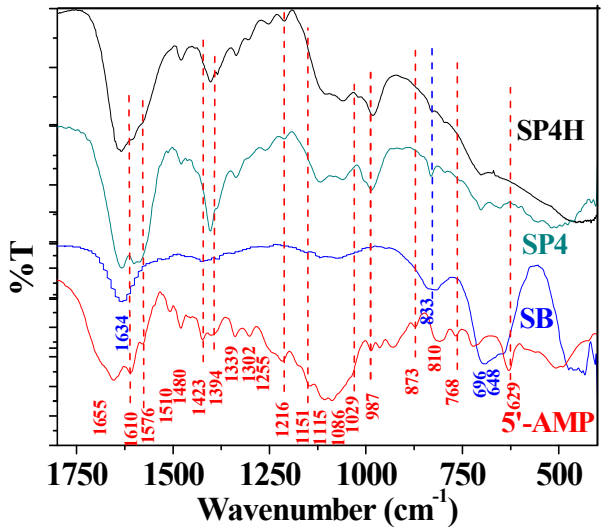

Fig. 15 FTIR spectra of SB, SP4 and SP4H along with 5'-AMP.

3.9 XPS analysis

The surface analysis of nanostructures in SP4H was carried out by recording its XPS spectrum in the binding energy range of 0–800 eV (Fig. 16 and Table S2). It shows various peaks due to different atomic species, the detailed analyses of peaks due to some of the major elements are presented in different panels. A doublet observed at 723.8 and 710.4 eV with a spin–orbit separation of 13.4 eV corresponds to Fe 2p electrons for Fe 2p(1/2) and Fe 2p(3/2) electrons, respectively (Fig. 16 (b)). Multiple peak fit analysis using software, XPSPEAK4.1 exhibit each of these peaks to split apart into two components with the spin orbit separation for both the pairs of peaks remaining the same (13.4 eV). It also shows a satellite peak at about 719.7 eV. The weaker peaks observed at 56.1 and 94.6 eV can be assigned to the Fe 3p and Fe 3s, respectively.

The peak corresponding to O 1s is observed at 531.0 eV, which could be fitted in to four components at 529.8, 531.1, 532.1 and 533.0 eV (Fig. 16 (d); Table S2). These peaks (eV) could be assigned to oxygen as O_2^- (529.8), OH^- (531.1), adsorbed H_2O (532.1), and –OH in 5'-AMP (533.0). The peak at ~ 533.0 eV has earlier been observed for pure DNA.[41] The peaks observed at binding energy of 286.1, 399.5, 199.6 and 133.3 eV correspond to C 1s, N 1s, Cl 2p and P 2p, respectively. The presence of the peaks due to N and P supports the interactions of Fe (III) with the pyrimidine, imidazole and PO_3^-, respectively as observed in IR study (Table S1). Other weak bands observed at 22.5 and 3.1 eV can be assigned to the valence band spectrum (Fig. 16 (h)). The observed data are well in agreement to the reports on β–FeOOH phase.[42,43]

3.10 Magnetic measurements

In view of the enhanced porosity observed in case of SP4H, the magnetic properties of both fresh (SP4) and aged (SP4H) samples were examined. The magnetic hysteresis loops for SP4 up to ±7 T are presented in Fig. 17 (a) at different temperatures varying from 300 K to 5 K. At 300 K, the magnetization curve exhibits superparamagnetic behavior having zero Mr and Hc with the magnetization value of 3.2 emu/g at 7 T. A decrease in temperature to 100 K also did not bring any change in the magnetic nature of these nanostructures but enhanced the limiting magnetization to 7 emu/g. Moreover, the magnetization started to attain the limiting value. A further reduction in temp to 5 K exhibits both remanance (Mr) (0.65 emu/g) and the coercivity (Hc) (0.16 T) indicating the ferromagnetic behavior of SP4 at 5 K along with an increase in the magnetization to 11.2 emu/g. Such a behavior is in contrast to bulk β-FeOOH which is known to be antiferromagnetic.[2]

The hysteresis loops for SP4H were recorded at different temperatures 300, 100 and 10 K upto ±7 T and are shown in Fig. 18 (a). The magnetization curves recorded at 300 K exhibit superparamagnetic behavior with a magentization of ~3.4 emu/g at 7 T without reaching any plataue value. Upon decreasing the temperature to 100 K, it starts to attain plataue value and still shows superparamagnetic behavior associated with an increase in magnetization to ~7 emu/g. However, a further decrease in temperature to 10 K results in an irreversible hysteresis loop suggesting a change in its magentic behavior from superparamagnetic to ferromagnetic. From the hysteresis loop the value of Mr and Hc were obtained to be about 0.5 emu/g and 0.1 T, respectively. The hysteresis loops recorded at different temperatures were magnified in small field range of ± 0.25 T (Fig. 18 (b)). It clearly reveals superparamagnetic behavior of the plots recorded at 300 and 100 K with the absence of Mr and Hc, whereas the curve at 10 K exhibited Mr and Hc without any exchange bias effect.

FC-ZFC curves for SP4H were recorded at an external field of 100 Oe in the temperatures range of 10 to 300 K (Fig. 19). At 100 Oe it exhibits maxima in ZFC curve at 39.6 K which has been

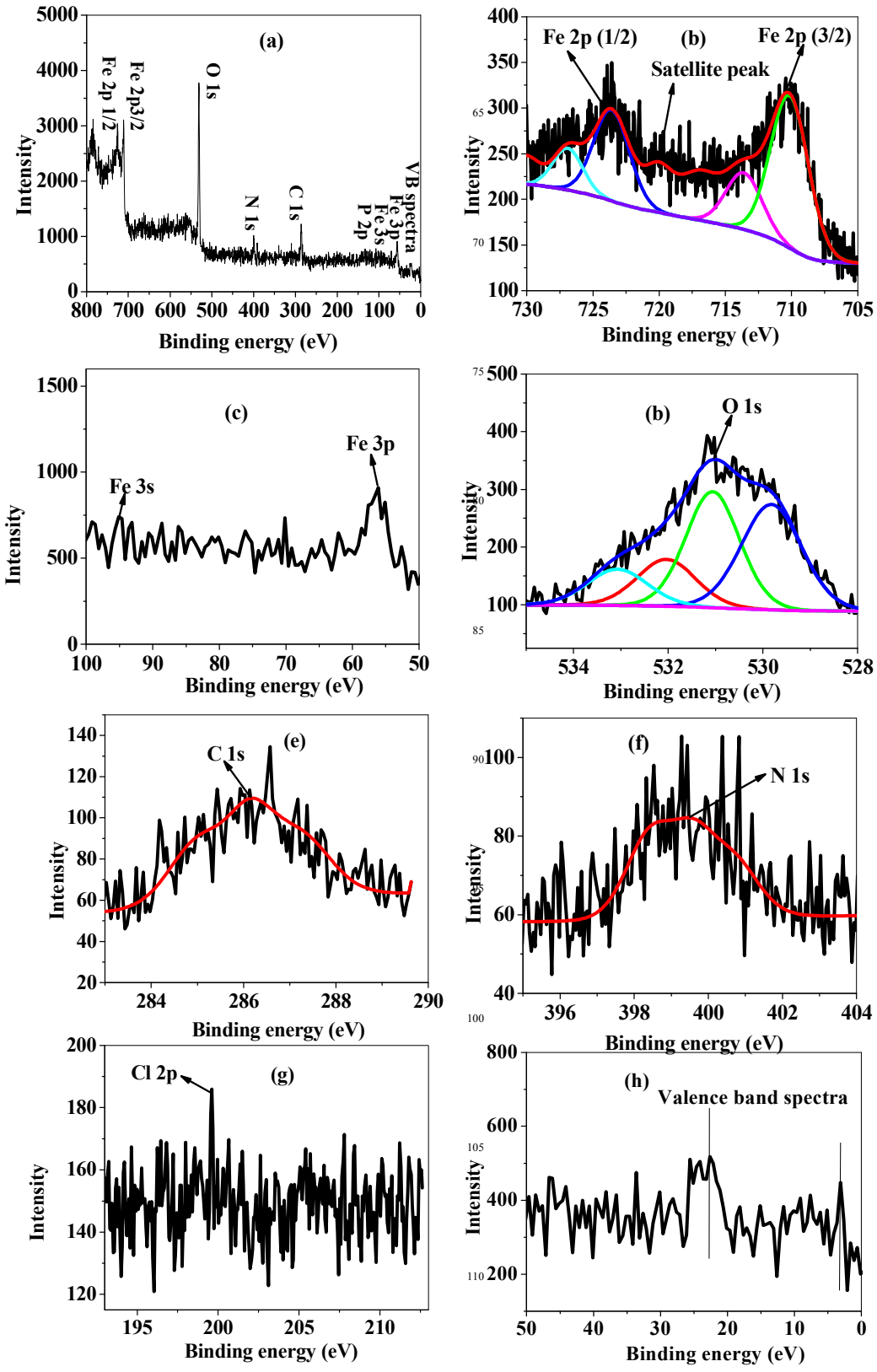

Fig. 16 XPS plots for SP4H: Full scale (a); Fe 2p (b); Fe 3s and 3p (c); O 1s (d); C 1s (e); N 1s (f); Cl 2p (g) and valence band spectrum (h).

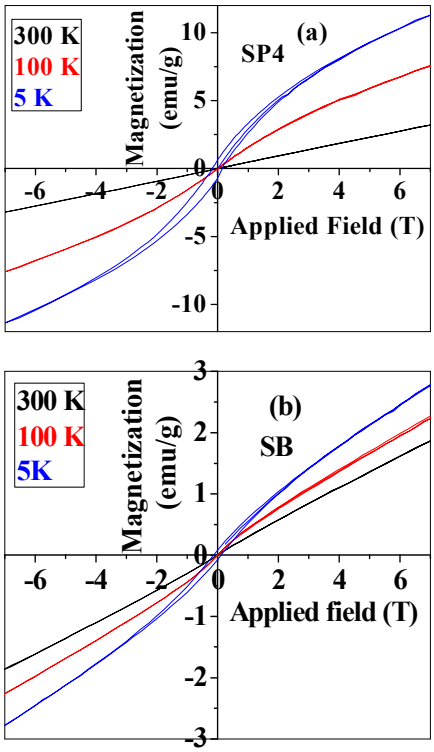

Fig. 17 M-H loop for SP4 (a) and SB (b) at various temperatures: 300, 100 and 5 K.

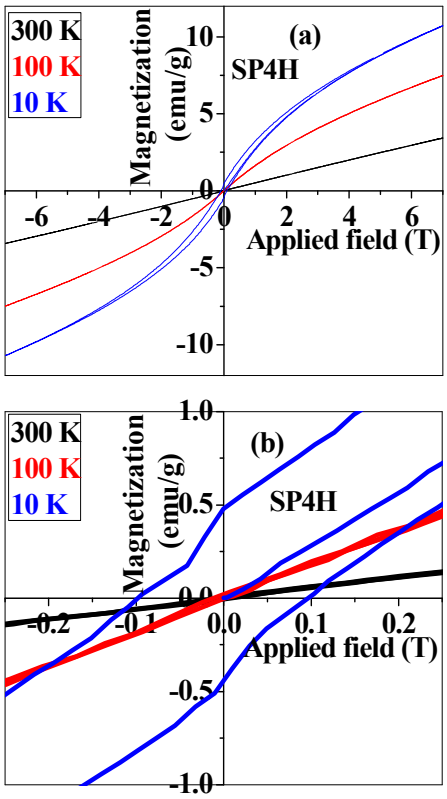

Fig. 18 (a) M-H loop for SP4H at various temperatures: 300, 100 and 5 K; (b) magnified M-H loop for SP4H.

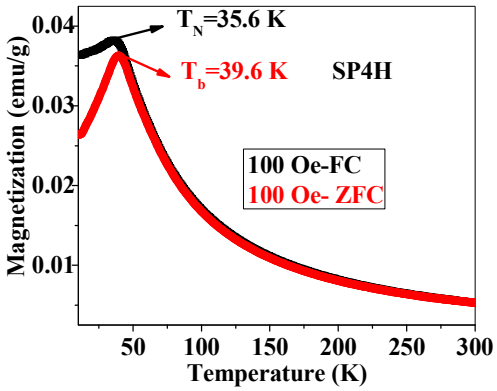

Fig. 19 FC-ZFC plots for SP4H recorded at an external field of 100 Oe.

assigned as blocking temperature (T_b) for this curve. Above this temperature these nanostructures exhibit superparamagnetic nature and below this temperature the spin are blocked by the magnetic anisotropy. A broad peak is observed in the FC curve with a maximum at 35.6 K which corresponds to the magnetic anisotropy temperature, T_N.

4. Discussion

The iron oxide phase in SP4 was identified to be β-FeOOH by Raman, SAED, IR and XPS analyses (Figs. 3, 11(d), and 16). SAED analysis of SP4 and SP4H indicated them to be present in the amorphous phase (Figs. 11 (d) and 12 (d)). Since any shorter or longer refluxing time than 6 h yielded the less intense peaks due to β-FeOOH phase (Fig. 3a). For refluxing time of > 6 h, it is likely to get converted into the mixed phase(s), as was observed for adenine templated β-FeOOH nanostructures.[36]

SP4 is considered to consist of building blocks in which β-FeOOH is present in the core and is coated by 5'–AMP present in the shell. This hypothesis is also indicated by optical absorption spectroscopy, in which an increase in the concentration of 5'–AMP results in the simultaneous decrease in the absorption below 430 nm associated with an increase in absorption in the longer wavelength range (Fig. 4(a)). These changes have been understood by the increased masking of β-FeOOH phase by 5'–AMP in the building block, resulting in the smaller absorption coefficient below 430 nm and enhancing the ligand field transition beyond 430 nm due to Fe^{3+} because of the increased Fe^{3+}– Fe^{3+} interactions. However, this spectrum is quite different to that observed for α–Fe_2O_3, for which a fairly intense band is observed at 430 nm.[39] Although the capping by 5'–AMP results in the appearance of 260 nm band due to 5'–AMP, but its increasing amount does not result in the higher absorption (Fig. 4a). This finding is understood by the fact that increased 5'–AMP masks the absorption due to β-FeOOH phase, as is noted by a reduction in the absorption for SP1-SP5 in the entire recorded UV-visible absorption range. Upon aging of SP4 the changes in the optical absorption were very similar to those observed upon increasing the [5'–AMP] (Fig. 5(a)). Obviously, aging results in the reorganization of 5'-AMP molecules present in the shell leading to the enhanced supramolecular interactions among Fe^{3+} centers within the building block resulting in an increased absorption in NIR region along with a simultaneous decrease in UV-Visible

region exhibiting an isosbestic point at about 430 nm. These nanoparticles and in particular the hydrogel exhibited fairly high absorption in NIR region (750-1100 nm), where tissues do not have any absorption, suggest the applications of these nanostructures as contrast agent for photoacoustic imaging and MRI.[44] The changed interactions between the template and the core β-FeOOH upon aging are also supported by IR and Raman spectroscopic data.

The observed changes in IR spectra of SP4 and SP4H (Fig. 15) suggest an increased interaction(s) involving β-FeOOH and 5'-AMP as well as 5'-AMP - 5'-AMP causing a significant reduction in the intensity of the O-H···Cl deformation and Fe-O-Fe stretching peaks observed at 830, and 701 and 648 cm^{-1}, respectively. These observations can be understood by the increased supramolecular interactions among different building blocks upon gelification involving β-FeOOH and 5'-AMP and 5'-AMP - 5'-AMP. The peaks due to β-FeOOH are masked and 5'-AMP gets diminished and slightly red shifted. Whereas, in Raman spectrum of SP4H peaks due to 5'-AMP become more prominent (Fig. 3).

In XPS analysis of SP4H the peak observed at 710.4 eV is characteristic of the Fe^{3+} component(s) and shows the absence of the Fe^{2+} component(s), which have binding energy of about 708.5 eV (Fig. 16 (b)).[45] Further, the presence of a satellite peak at about 719.7 eV in the binding energy spectrum of SP4H is different to that observed for Fe_3O_4, where no such peak is observed.[46] Moreover, this spectrum is markedly different to those of α–FeOOH and γ–Fe_2O_3.[45,47] The present XPS pattern matches fairly well to those reported for β–FeOOH phase,[42,43] and thus confirming the production of iron oxide as β–FeOOH phase in SP4H. The appearance of the peaks at binding energy of C, N, O and P shows the presence of 5'–AMP in SP4H.

The reorganization in SP4 upon aging are clearly evidenced by DLS measurements in which the value of ζ-potential shows a regular change from + 45 mV to - 35 mV associated with an increase in pH from 4.0 to 8.0. At physiological pH of 7.2 it exhibits ζ-potential of ~ - 29.7 mV. Based on the overall negative charge observed in the pH range > 4, the interaction of iron through phosphate ion of 5'-AMP will predominate. It thus produces the negatively charged species upon aging. The generation of porosity in SP4H, as was revealed by FESEM, TEM and AFM images, can also be appreciated by increased interaction among 5'-AMP and their decreased interactions with the core β-FeOOH. Based on the above observations the structure of SP4H is shown in Scheme 2.

The increase in the magnetization value for SP4 and SP4H as compared to SB is understood due to the change in the surface spin upon co-ordination of β-FeOOH with 5'-AMP (Figs. 17 and 18). The superparamagnetic nature of SP4H was further examined by recording the FC-ZFC curves at higher external field of 500 Oe, which resulted in a decrease in the T_b value to 38.9 K from 39.6 K at 100 Oe (Figs. 19 and 20). Such a decrease in the value of T_b in ZFC curve suggests SP4H to be superparamagnetic and supports the above observations.[48]

A low value of T_b can be understood due to reduction in surface spin and broken exchange because of coordination of Fe with 5'-AMP associated with an increase in magnetization. A drastically lower value of T_N (35.6 K) in FC curve as compared to that of bulk material (297 – 300 K) indicates the nature of β-FeOOH in SP4H to be amorphous[49] as is also indicated by SAED analysis. A further increase in applied field to 500 Oe changes its shape from the broad peak to kink without affecting appreciably the T_N value.

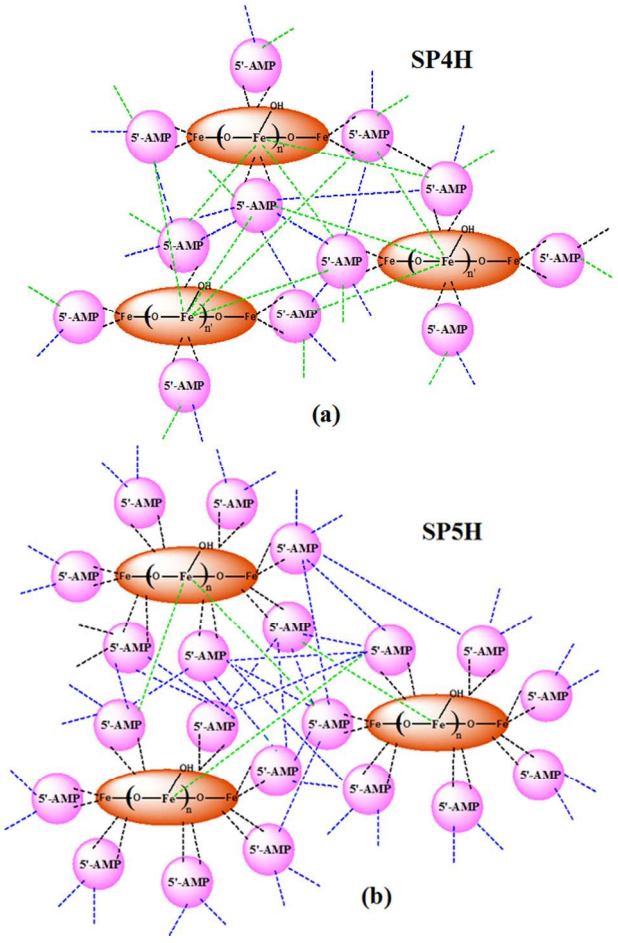

Scheme 2 The supramolecular interactions involved in SP4H and SP5H: 5'–AMP–core β–FeOOH (**black**); 5'–AMP–neighbouring β–FeOOH (**green**) and 5'–AMP–5'–AMP (**blue**).

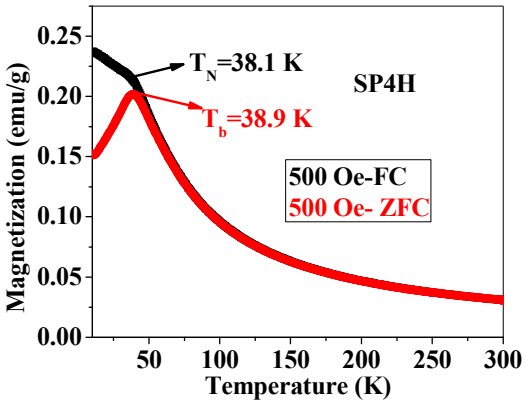

Fig. 20 FC-ZFC plots for SP4H recorded at an external field of 500 Oe.

In order to verify the superparamagnetic nature of β-FeOOH in SP4H, the plots of M vs. H/T using the data from the M-H (Fig. 18 (a)) and FC curves (Figs. 19 and 20) at different temperatures and applied fields were plotted (Fig. 21). The data were taken in

the applied field and temperature range of ±1T and 300-50 K, respectively. All the data points from the different plots superimpose on to the same curve (Fig. 21). It clearly supports the superparamagnetic nature of β-FeOOH nanostructures in SP4H up to 50 K.[50] Whereas, the M vs. H/T plot obtained at 10 K shows completely different behavior to those of at higher temperatures (Fig. S6). The non-superimposition of plots at 10 K can be attributed to the change in the magnetic nature from superparamagnetic to ferromagnetic below 50 K.

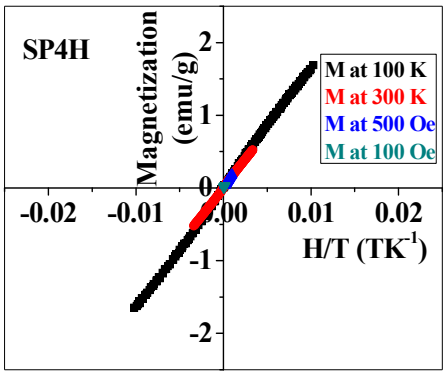

Fig. 21 Magnetization *vs* H/T plots for SP4H at 100 and 300 K for applied field up to ±1 T and at 0.0100 and 500 Oe up to 50 K.

Thus the used biotemplate influences the surface spin through co-ordination, which is reflected by enhanced magnetization. This is remarkable to note that the 5'-AMP – mediated hydrogel encapsulating β-FeOOH could be obtained by employing fairly low concentration of 5'-AMP without using any external gelator, as compared to the previously reported 5'-AMP based hydrogels at high concentration of 5'-AMP (0.8 wt%) using alkaline phosphatase enzyme as gelator.[31] The viscoelastic properties of these gels exhibiting relatively higher mechanical strength at lower concentrations of 5'-AMP are interesting. The rheological properties and dye/drug loading and release capabilities of the hydrogel are very interesting and are presently under investigation and will be reported elsewhere.

The above observed characteristic features such as porosity, NIR absorption, relatively high surface area and superparamagnetic behavior of the optimized sample, consisting of relatively non-toxic components, suggest it to qualify as green material having potential for biomedical applications.

5. Conclusion

We have for the first time synthesized 5'-AMP mediated β-FeOOH hydrogel at physiological pH. The presence of β-FeOOH in has been confirmed from the Raman, UV-Visible spectroscopy, and SAED analysis. The surface analysis of the nanostructures in SP4H by XPS shows the presence of Fe as Fe^{3+} only and also ruled out the presence of Fe_3O_4 phase. The presence of phosphate group and sugar moiety in 5'-AMP is responsible for gelification. The interaction of nucleotide with the inorganic core consisting β-FeOOH could be manipulated by a change in the reaction parameters like pH, temperature and chemical environment. The amount of 5'-AMP controlled the morphology of the nanostructures, about 2.5 mM of 5'-AMP resulted in the transformation of morphology from nanorods to spherical nanoparticles results in the formation of porous hydrogel in the process of self-assembly. The increased supramolecular interactions are found to be responsible for the formation of porous hydrogel as evidenced by IR spectroscopy. The magnetic studies reveal that coating of these materials by biomolecules resulted in the formation of superparamagnetic nanostructures with more than 75% of increase in the magnetization at room temperature. The interesting features of the as synthesized biotemplated porous β-FeOOH hydrogel with multifunctional properties viz. NIR absorption, enhanced magnetization, superparamagnetic behavior at room temperature having biocompatible components (β-FeOOH and 5'-AMP) suggests their potential for various biological applications.

Acknowledgements

Financial support of CSIR, New Delhi (Grant no. CSR-780-CMD), to undertake this work is gratefully acknowledged. S.K.G. is thankful to MHRD, New Delhi, for the award of SRF. Thanks are also due to the Head IIC, IITR, Roorkee, for providing the facilities of FESEM and TEM.

Notes and references

Departmetn of Chemistry, Indian Institute of Technology Roorkee, Roorkee-247667, Uttarakhand, INDIA.
E-mail:anilkfcy@iitr.ac.in; akmshfcy@gmail.com

† Electronic Supplementary Information (ESI) available: EDAX analysis of SP4H at different marked locations in images A and B and their corresponding elemental distribution (Fig. S1), Size distribution histogram of diameter of spherical nanoparticles in SP3 and SP5 (Fig. S2), Size distribution histogram of length and diameter of nanorods in SP3, SP4 and SP5 (Fig. S3), Interactive 3D surface plot of the TEM image of the SP4H (Fig. S4), AFM image of the fresh samples and their respective 3D images: SP3 (a) and (a'); SP4 (b) and (b') and SP5 (c) and (c') (Fig. S5), Magnetization *vs* H/T plots for SP4H at 100 and 300 K for applied field up to ±1 T and at 100 and 500 Oe up to 50 K including data point from M-H curve recorded at 5 K at ± 1T (Fig. S6), IR spectral data of 5'-AMP, β-FeOOH (SB, SP4 and SP4H) (Table S1) and The XPS analysis data of SP4H (Table S2).
See DOI: 10.1039/b000000x/

References

1. R. Zboril, M. Mashlan and D. Petridis, *Chem. Mater.*, 2002, **14**, 969.
2. R. M. Cornell and U. Schwertmann, *The iron oxides— structure, properties, reactions, occurrences and uses*, WileyVCH, Darmstad, 2003.
3. S. Laurent, D. Forge, M. Port, A. Roch, C. Robic, L. V. Elst and R. N. Muller, *Chem Rev.*, 2008, **108**, 2064.
4. A. K. Gupta and Gupta M, *Biomaterials*, 2005, **26**, 3995.
5. D. Ling, and T. Hyeon, *Small*, 2013, **9**, 1449.
6. Z. Pu, M. Cao, J. Yang, K. Huang and C. Hu, *Nanotechnol.*, 2006, **17**, 799.
7. S. Jiao, L. Xu, K. Hu, J. Li, S. Gao and D. Xu, *J. Phys. Chem. C*, 2010, **114**, 269.
8. S. Kakuta, T. Numata and T. Okayama, *Catal. Sci. Technol.*, 2014, **4**, 164.
9. C. Dong, Z. Yan, J. Kokx, D. B. Chrisey and C. Z. Dinu, *App. Surf. Sc.*, 2012, **258**, 9218.
10. C. Dong, A. S. Campell, R. Eldawud, G. Perihinschi. Y. Rojanasakul, C. Z. Dinu, *App. Surf. Sc.*, 2013, **264**, 261.
11. Nakamura, Acicular Magnetic Iron Oxide Particles and Magnetic Recording Media Using Such Particles,US Pat., Pat. no. 5120604, 1992.
12. Y. Tian, B. Yu, X. Li and K. Li, *J. Mater. Chem.*, 2011, **21**, 2476.

13. L.-P. Zhu, L.-L. Wang, N.-C. Bing, C. Huang, L.-J. Wang and G.-H. Liao, *ACS Appl. Mater. Interfaces.*, 2013, **5**, 12478.
14. Z. Zhou, L. Wang, X. Chi, J. Bao, L. Yang, W. Zhao, Z. Chen, X. Wang, X. Chen and J. Gao, *ACS Nano*, 2013, **4**, 3287.
15. L. M. Rossi, N. J. S. Costa, F. P. Silva and R. Wojcieszak, Green Chem., 2014, 16, 2906.
16. M. Cano, K. Sbargoud, E. Allard and C. Larpent, *Green Chem.*, 2012, **14**, 1786.
17. C. Tassa, S. Y. Shaw and R. Weissleder, *Acc. Chem. Res*., 2011, **44**, 842.
18. A. Funabiki, H. Yasuda and M. Yamachi, *J. Power Sources*, 2003, **290**, 119.
19. E. A. Deliyanni, E. N. Peleka and K. A. Matis, *Sep Sci Technol.*, **42**, 993.
20. G. Z. Kyzas, E. N. Peleka and E. A. Deliyanni, *Materials*, 2013, **6**, 184.
21. F. Kolbe, H. Weiss, P. Morgenstern, R. Wennrich, W. Lorenz, K. Schurk, H. Stanjek and B. Daus, *J. Colloid Inter. Sc*., 2011, **357**, 460.
22. A. Kumar and V. Kumar, *Chem. Rev*., 2014, **114**, 7044.
23. A. Kumar and S. K. Gupta, *J. Mater. Chem. B*, 2013, **1**, 5818.
24. J. Coffer and S. Bigham, J. Cluster Science, 2000, 11, 359.
25. J. L. Coffer, S. R. Bigham, X. Li, R. F. Pinizzotto, Y. G. Rho, R. M. Pirtle and I. L. Pirtle, *Appl. Phy. Lett.*, 1996, **69**, 3851.
26. M. –L. Chen, L. –M. Shen, S. Chen, H. Wang, X. W. Chen and J.-H. Wang, *J. Mater. Chem. B*, 2013, **1**, 2582.
27. L. Zeng, W. Ren, J. Zheng, A. Wu and P. Cui, *Appl. Surf. Sci*., 2012, **258**, 2570.
28. M. Babic, D. Horák, M. Trchová, P. Jendelová, K. Glogarová, P. Lesný, V. Herynek, M. Hájek and E. Syková, *Bioconjugate Chem*., 2008, **19**, 740.
29. A.-H. Lu, E. L. Salabas and F. Schüth, *Angew. Chem. Int. Ed.*, 2007, **46**, 1222.
30. M. Mahmoudi, S. Sant, B. Wang, S. Laurent and T. Sen, *Adv. Drug Delivery Rev*., 2011, **63**, 24.
31. X. Du, J. Li, Y. Gao, Y. Kuang and B. Xu, *Chem. Commun*., 2012, **48**, 2098.
32. K. Roy, C. P. Vinod and C. S. Gopinath, *J. Phys. Chem. C*, 2013, **117**, 4717.
33. L. Bellot-Gurlet, D. Neff, S. Reguer, J. Monnier, M. Saheb and P. Dillmann, *J. Nano Res.*, 2009, **8**, 147.
34. S. Das and M. J. Hendry, *Chemical Geology*, 2011, **290**, 101.
35. J. Kundu, O. Neumann, B. G. Janesko, D. Zhang, S. Lal, A. Barhoumi, G. E. Scuseria and N. J. Halas, *J. Phys. Chem. C*, 2009, **113**,14390.
36. A. Kumar and S. K. Gupta, *J. Nanopart. Res.*, 2013, **15**, 1466.
37. S. Chatterjee, S. Sarkar and S. N. Bhattacharyya, *J. Photochem. Photobiol. A Chem*, 1993, **72**,183.
38. H. Maeda and Y. Maeda, *Langmuir*, 2011, **27**, 2895.
39. D. M. Sherman and T. D. Waite, *American Mineralogist*, 1985, **70**, 1262.
40. H.-A. Tajmir-Riahi, *Biochimica et Biophysica Acta*, 1989, **1009**, 168.
41. C.-Y. Lee, P. Gong, P., G. M. Harbers, D. W. Grainger, D. G. Castner and L. J. Gamble, *Anal. Chem*., 2006, **78**, 3316.
42. H. Mao, X. Lu, D. Chao, L. Cui, Y. Li and W. Zhang, *J. Phys. Chem. C*, 2008, **112**, 20469.
43. M. Ding, B. H. W. S. D. Jong, S. J. Roosendaal and A. Vredenberg, *Geochim. Cosmochim. Acta*, 2000, **64**, 1209.
44. P.-H. Ting, C.-C. Huang and M.-L. Li, Proc. SPIE 8943, Photons Plus Ultrasound: Imaging and Sensing 2014, doi:10.1117/12.2037448.
45. T. Fujii, F. M. F. de Groot and G. A. Sawatzky, *Phys. Rev. B*, 1999, **59**, 3195.
46. Y. Tian, B. Yu, X. Li and K. Li, *J. Mater. Chem*., 2011, **21**, 2476.
47. H. Abdel-Samad and P. R. Watson, *Appl. Surf. Sci*., 1997, **108**, 371.
48. P. Prené, E. Tronc, J.-P. Jolivet, J. Livage, R. Cherkaoui, M. Noguks and J.-L. Dormann, *IEEE TRANS. MAGN.*, 1993, **29**, 2658.
49. L.-Y. Zhang, D.-S. Xue and J. Fen, *J. Magn. Magn. Mater*., 2006, **305**, 228.
50. K. J. Klabunde, *Nanoscale materials in chemistry*, John Wiley & Sons, Inc., 2001.

Graphical Abstract

Supramolecular–directed novel superparamagnetic 5'-adenosine monophosphate templated β-FeOOH hydrogel with enhanced multi-functional properties

Anil Kumar and Sudhir Kumar Gupta

Superparamagnetic 5'-AMP-mediated β-FeOOH porous hydrogel containing non-toxic components with high surface area, NIR absorption with potential utility for biomedical applications.